J Mater Sci (2010) 45:783–792
DOI 10.1007/s10853-009-4001-y

Calibration of reaction parameters for the improvement of thermal stability and crystalline quality of multi-walled carbon nanotubes

Saveria Santangelo · Giacomo Messina · Giuliana Faggio · Maurizio Lanza · Alessandro Pistone · Candida Milone

Received: 23 July 2009 / Accepted: 28 October 2009 / Published online: 11 November 2009

Abstract The results of Raman analysis on multi-walled carbon nanotubes, prepared by catalysed chemical vapour deposition, are used as a guide for the calibration of the growth parameters, directed to improve crystalline quality and resulting thermal stability of nanotubes. Under selective growth conditions, the resistance to oxidation in air, as assessed by thermogravimetry measurements, is found to increase with the establishment of the long-range graphitic order in radial tube direction, as signalled by the Raman G′/G intensity ratio enhancement. In the range of parameters explored (synthesis temperature: 500–700 °C; growth atmosphere: 120 cc/min *i*-C_4H_{10}–H_2–He mixture with He at 0–25%; *i*-C_4H_{10}/H_2 flow ratio: 1–3; metal load and reduction temperature of Fe/Al_2O_3 catalysts: 17–40 wt%, and 500 and 700 °C, respectively), the best crystalline quality and the highest oxidative resistance are achieved by carrying out the synthesis reaction at 700 °C in 1:1:0 *i*-C_4H_{10}–H_2–He atmosphere over 29 wt% Fe catalysts reduced at 700 °C. An additional relevant finding is the strong correlation evidenced between results of thermogravimetry and Raman analyses, suggesting the use of Raman spectroscopy for *non-destructively* evaluating the thermal stability of any graphitically ordered carbon species.

S. Santangelo (✉) · G. Messina · G. Faggio
Dipartimento di Meccanica e Materiali, Facoltà di Ingegneria, Università "Mediterranea", 89122 Feo di Vito, Reggio Calabria, Italy
e-mail: saveria.santangelo@unirc.it

M. Lanza
C.N.R., Istituto per i Processi Chimico-Fisici Sez. Messina, 98158 Faro Superiore, Messina, Italy

A. Pistone · C. Milone
Dipartimento di Chimica Industriale e Ingegneria dei Materiali, Facoltà di Ingegneria, Università di Messina, 98166 Messina, Italy

Introduction

From their first observation (1991) as by-product in the synthesis of fullerenes [1], carbon nanotubes (CNTs) have gathered increasing scientific interest in an interdisciplinary research ambit. In recent years, besides as excellent emitters [2], CNTs have acquired great strategic importance for a large variety of different advanced technology applications ranging from hydrogen storage [3] to biosensing [4], and from nanomachining [5] to tissue engineering [6].

A lot of methods are successfully utilised for their preparation [7]. High yields are mandatory for their production on industrial scale, whereas the prerequisites the synthesised CNTs have to satisfy may be even appreciably different depending on the specific employment field. Several applications require good crystalline quality and high resistance to oxidation [8].

Raman spectroscopy (RS) is widely utilised to investigate the crystalline arrangement of carbonaceous deposits, while their thermal stability is evaluated by thermogravimetry (TG). Thanks to the latest advances in the study of oxidation, detailed additional information on the specimen composition can be, in principle, inferred by comparatively analysing the results of high-resolution TG and the indications provided by electron microscopy [9–11]. However, Gozzi et al. [12] have recently pointed out that the capability of discriminating amongst various carbon forms markedly reduces when TG measurements are carried out, as usually, in pure oxygen or oxygen containing mixtures. More reliable information on the relative CNT abundance

in a carbonaceous matrix can be deduced through use of TG in a pure CO_2 atmosphere under the operating conditions of the Boudouard reaction catalysed by suitable oxides (such as Cr_2O_3) [12].

This article deals with the catalysed chemical vapour deposition (CCVD) growth of multi-walled carbon nanotubes (MWCNTs) in 120 cc/min i-C_4H_{10}–H_2–He atmosphere over Fe/Al_2O_3 catalysts. Attention is chiefly focused on the achievement of thermal stability adequate to the potential use of CNTs in oxidative environment. This objective is pursued by properly tuning the growth parameters (synthesis temperature: 500–700 °C; i-C_4H_{10}/H_2 flow ratio: 1–3; He fraction: 0–25%; metal load: 17–40 wt%; catalyst reduction temperature: 500 and 700 °C) on the basis of the indications, concerning crystalline arrangement and oxidative resistance, respectively provided by RS and conventional TG in air, with the aid of the results of analyses of the reaction product morphology by scanning electron microscopy (SEM) and high-resolution transmission electron microscopy (HRTEM).

In the search for optimal growth conditions, in addition to the concentration of Fe-catalyst impurities (3.5–53.2%), only the relative abundance of the (graphitically-ordered/disordered) species, whose oxidation occurs in well distinct temperature ranges, is quantitatively evaluated (41.6–95.9%/0.6–5.2%). Instead, no quantitative TG-based estimation (but only a qualitative SEM-based evaluation) of the relative amounts is attempted for those (MWCNTs and graphitic flakes) here showing comparable reactivity. Notwithstanding this, the picture emerging is that, thanks to the clear correlation with the results of TG measurements, the outcomes of Raman analysis on the carbonaceous products, used to tune the preparation conditions and to drive the growth process towards the achievement of well-crystallised thermally-stable nanotubes, can be helpful for a preliminary non-destructive evaluation of the resistance to oxidation of any species with graphitic ordering.

Experimental details

Preparation of catalysts and samples

Catalysts are prepared by impregnation method. Al_2O_3 grains (nominal size: 75–125 μm) are wetted in an aqueous solution of $Fe(NO_3)_3 \cdot 9H_2O$ with proper Fe concentration. After drying at 120 °C and calcination at 750 °C, catalyst precursor is reduced for 1 h upon 60 cc/min H_2 flow. Metal loads (w_M) and reduction temperatures (T_R) are reported in Table 1.

Afterwards, 500 mg of reduced catalyst is placed in a quartz boat inside the reactor. The reactor is a 50-mm diameter, 700-mm-long quartz tube; it is located in a horizontal electric furnace, where the catalyst is heated upon 120 cc/min H_2–He flow up to synthesis temperature (T_S). As T_S is reached, He is partially or wholly replaced by i-C_4H_{10}, keeping constant the total gas flow. The reaction is stopped after 2 h. Growth ambient composition and reaction temperature are indicated in Table 1, together with the amount of C deposits per gram of catalyst (Y_C) correspondingly attained.

Sample purification and diagnostics

After reaction, the raw products are cooled down to room temperature (RT) in He atmosphere. Al_2O_3 support and residual Fe-particles are removed by 1 M solutions of NaOH and HCl, respectively. C deposits are then washed in distilled water and dried at 110 °C. Finally, the so-purified products are examined by routinely used diagnostic techniques.

The crystalline quality is evaluated by RS. Raman scattering, excited by an Ar^+ laser (Coherent Innova 70) operating at 2.41 eV, is measured at RT in the 800–3350 cm^{-1} spectral range by using a double monochromator (Jobin–Yvon Ramanor U-1000) equipped with a microscope

Table 1 Sample preparation conditions: metal load (w_M) and reduction temperature (T_R) of Fe/Al_2O_3 catalyst, flow rates of reactive gases ($\Phi_{i-C_4H_{10}}$ and Φ_{H_2}) and synthesis temperature (T_S)

Sample code	w_M (wt%)	T_R (°C)	$\Phi_{i-C_4H_{10}} + \Phi_{H_2}$ (cc/min)	T_S (°C)	Y_C (%)
#A	29	700	60 + 60	700	1434.0
#B	29	700	60 + 30	600	293.8
#C	29	700	60 + 60	600	438.5
#D	29	500	60 + 60	600	912.8
#E	29	700	90 + 30	600	294.8
#F	40	500	60 + 60	600	515.5
#G	17	500	60 + 60	600	827.7
#H	29	700	60 + 60	500	299.0

In all the experiments, the flow rate of i-C_4H_{10}–H_2–He mixture is 120 cc/min. The results attained in terms of yield to C deposits (Y_C) are also shown. Samples are labelled in decreasing thermal-stability order

(Olympus BX40, ×50 objective) and a photomultiplier (Hamamatsu R943-02) operating in photon-counting mode. Aiming at a reliable description of the sample bulk, several different locations of each specimen are sampled on account of the possible structural non-homogeneity. A 30-s long acquisition time is used to improve the S/N ratio, while the use of a very low power density at the sample surface ($<1 \times 10^5$ W/cm^2) prevents thermal annealing effects [13]. Spectra recorded are then normalised and averaged.

The thermal stability and purity degree are investigated by TG (TA Instruments SDTQ600) analysing the 200–1000 °C temperature range. A very low scan rate (1 °C/min) is chosen in order to ensure a good experimental reproducibility, otherwise hindered by significant time lag between furnace temperature and sample temperature and by auto-combustion effects. 2–5 mg of each sample, preliminarily kept at 200 °C in inert ambient until balance-response stabilisation, are burned in 100 cc/min air flux.

Finally, the morphology is observed by SEM (JEOL JSM-5600LV) and HRTEM (JEOL JEM-2010, equipped with a Gatan 794 Multi-Scan CCD camera).

Further technical details concerning measurements performed and instrumentation utilised can be found elsewhere [14–16].

Criterion for the choice of growth parameters

Previous studies concerning the MWCNT growth by the use of 120 cc/min C_2H_6–H_2 mixture and Fe/SiO_2 catalysts indicated 1:1 as the hydrocarbon:hydrogen flow ratio giving the highest yield with still-satisfactory selectivity and crystalline quality [15, 16]. On the basis of these results, samples (#A, #C–D and #F–H) used for calibrating metal load and reduction temperature of Fe/Al_2O_3 catalysts, as well as synthesis temperature, are prepared in 1:1 i-C_4H_{10}–H_2 atmosphere without He addition. Metal load is first tuned. Catalysts used for this purpose are reduced at 500 °C. Once adjusted w_M, a higher T_R is considered. In both the cases, reaction is carried out at moderate (600 °C) temperature. The influence of synthesis temperature and of growth ambient composition (samples #A–C, #E and #H) on the CNT quality is investigated, using the catalyst preparation conditions ($w_M = 29$ wt% and $T_R = 700$ °C) under which, in previous steps, the best crystalline quality, as assessed by RS analysis, is achieved.

Results and discussion

Under the preparation conditions of Table 1, 3–14 g of C deposit per gram of catalyst is attained. The CNT formation is ascertained by the morphology examination by SEM (Fig. 1). However, the selectivity towards nanotubes seems strongly influenced by the choice of operating conditions. The accurate sample observation (even more than 20 SEM images, with diverse magnification factors, are taken for each specimen) evidences that, in some cases, graphitic plaquettes of various sizes (within the dashed contours in Fig. 1a–g) are present, in different amounts, along with filaments. Actually, some graphitic flake is clearly seen also while focusing the Raman optical microscope (Fig. 1g). In sample #H, besides numerous and large plaques, a moderate amount of relatively shorter tubes having diameters of hundreds of nanometres (indicated by arrows in Fig. 1e) is observed.

HRTEM reveals that the filamentous structures are MWCNTs (Fig. 2) grown via a "root-growth" mechanism (no Fe-nanoparticle located at the tube tip is seen).

Actually, the thermograms of all the samples show a remarkable mass loss in the temperature range (400–600 °C) where the oxidation of MWCNTs is currently reported to take place [17] (Fig. 3a). Since the preliminary sample heating at 200 °C grants the absence of water and/or solvents (purification residues), the slower mass loss in the 200–400 °C region indicates that small amounts (0.6–5.2%) of amorphous/disordered C species are co-produced [18]. Further information comes from the differential TG (DTG) curves (Fig. 3b). The peak (maximum oxidation rate) temperature (T_P) is currently regarded as a measure of the *sample* resistance to oxidation [17], while the peak FWHM (ΔT) can be thought of as an index of heterogeneity in the oxidation process. The results derived from conventional TG and DTG analysis operated in air are summarised in Table 2: x_{AS} stands for the relative abundance of amorphous/disordered C species as inferred from the mass loss in the 200–400 °C region of thermograms, while x_{EI} denotes the concentration of carbon-encapsulated Fe-nanoparticles as displayed by the mass percent of unburnt matter [14].

Sample #H is quite different and deserves a deeper discussion. The relative amount of Fe-impurities exceeds that of carbonaceous deposits. The mass loss below 400 °C is sharper, while the oxidation at higher temperature progresses in two steps, bearing out the co-existence of two distinct components with different thermal stability. Aiming at their identification, the combustion is stopped after the first DTG peak (located around 420 °C) and the morphology of the unburnt residues is examined. By this procedure, nanotubes are found to burn at lower temperature, thus giving rise to the weaker DTG contribution, while the main peak at 537 °C originating from the oxidation of terraced flakes-like formations with lateral dimension comparable to the CNT diameters. Indeed, on one hand, bearing in mind that lattice defects at the tube end and

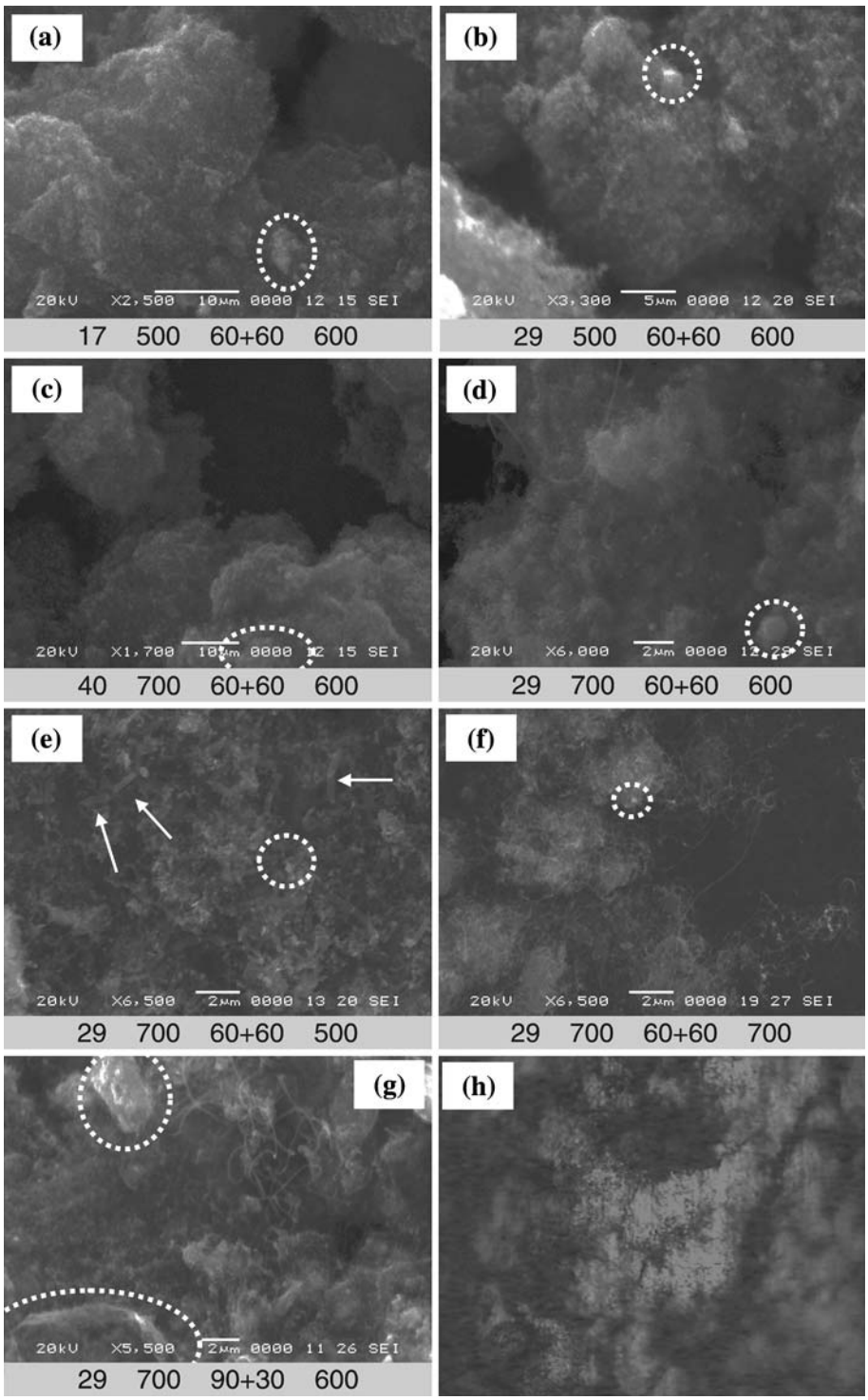

Fig. 1 **a–g** Selectivity towards nanotubes, as resulting from SEM analysis. The effects produced by the variation of metal load (**a–c**), catalyst reduction temperature (**b**, **d**), synthesis temperature (**d–f**) and growth ambient composition (**d**, **g**) are shown. At the bottom of each image, the corresponding preparation conditions are shown: metal load (wt%) and reduction temperature (°C) of catalyst, flow rates of reactive gases (i-C_4H_{10}+H_2, in cc/min) and synthesis temperature (°C). Along with filaments, specimens contain different amounts of graphitic terrace flakes (within the *white dashed contours*) having various sizes, which, in some case, seems clearly visible also by the Raman optical microscope (**h**). Besides plaquettes, tubes having diameters of hundreds of nanometres (*white arrows*) are observed in case (**e**)

along the outer walls act as initial oxidation sites [19, 20], it is easy to understand how the combustion of shorter tubes, with very large outer diameters and, hence, commensurately large wall surface exposed to the oxidative action of air, occurs at significantly lower temperatures.

On the other hand, this finding opens new problems related to the identification of the graphitically organised C phases with diverse morphology: the mass loss in the 400–600 °C temperature range gives the relative amount of *all* the C species with graphitic ordering (x_{GS} in Table 2), with *no possibility of reliable distinction* between the various morphologic components (here MWCNTs and plaques) whenever, as in case of samples #A–G, a single DTG peak is detected, owing to their comparable reactivity in air. As

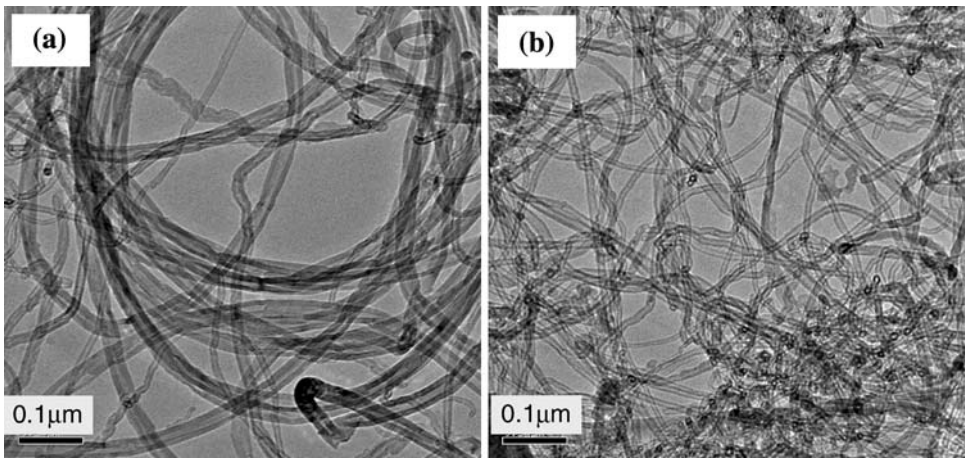

Fig. 2 TEM micrographs of MWCNTs exhibiting good crystalline quality and high thermal stability. Images refer to samples #A (**a**) and #C (**b**)

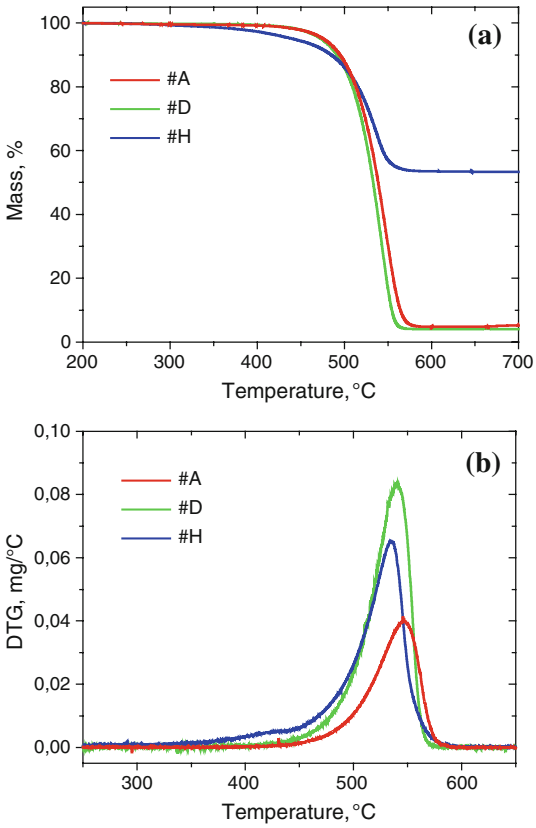

Fig. 3 Results of TG measurements: **a** Thermograms. **b** Differential TG curves of some samples

Table 2 Results of TG analysis: thermal stability, as measured by the peak temperature (T_P) in the DTG curves, and relative abundance of graphitically organised (x_{GS}) and of amorphous/disordered (x_{AS}) C species, as derived from the mass loss in the 400–600 °C and 200–400 °C regions of thermograms, respectively

Sample code	T_P (°C)	ΔT (°C)	x_{GS} (%)	x_{AS} (%)	x_{EI} (%)
#A	562.0	27.5	94.4	0.6	5.0
#B	558.0	26.6	87.7	1.1	11.2
#C	557.9	23.9	91.2	1.5	7.3
#D	554.1	22.3	95.9	0.6	3.5
#E	552.5	34.9	84.2	0.6	15.2
#F	550.4	33.3	91.2	0.8	8.0
#G	547.6	33.3	88.6	0.9	10.5
#H	537.0	35.4	41.6	5.2	53.2

The concentration of carbon-encapsulated Fe-nanoparticles (x_{EI}) as well as the FWHM (ΔT) of the peak in DTG curves is also reported

in case of yield (Table 1), a large variableness (42–96%) is observed for x_{GS}.

The results of Raman scattering measurements are shown in Fig. 4. The changes in crystalline arrangement of C deposits produced by the variation of the growth conditions reflect in the shape evolution of the main spectral features: the G-band (1580 cm^{-1}), derived from the graphite-like in-plane optical mode; the D-band (1350 cm^{-1}), originating from lattice defects (vacancies, pentagons and heptagons) that break the basic graphene-layer symmetry [21, 22]; and its overtone, the G′-band (2700 cm^{-1}), which, conversely, is detected only in presence of long-range order, as in graphite [22] and in nanotubes constituted by a sequence of smooth graphene sheets [23].

After background subtraction, the spectral features are fitted to Lorentzian bands (Fig. 5a) and the integrated-intensity ratios are calculated. The results attained are shown in Fig. 5b. As usual [24], the D/G intensity ratio (I_D/I_G), which, for fixed excitation energy, increases with decreasing the in-plane correlation length [25, 26] (i.e. the mean inter-defect distance [26, 27]), is used to monitor the extent of structural defects. Instead, the G′/G intensity ratio ($I_{G'}/I_G$) is indicative of long-range order [24]. The overall sample quality improves with increasing the mean inter-defect distance and/or long-range graphitic order (i.e. with increasing G/D and/or G′/G ratios, respectively) and is, hence, pictorially described by the G′/D intensity ratio ($I_{G'}/I_D$) [24].

According to the above picture, the results of Fig. 5b indicate that the crystalline quality increases from sample

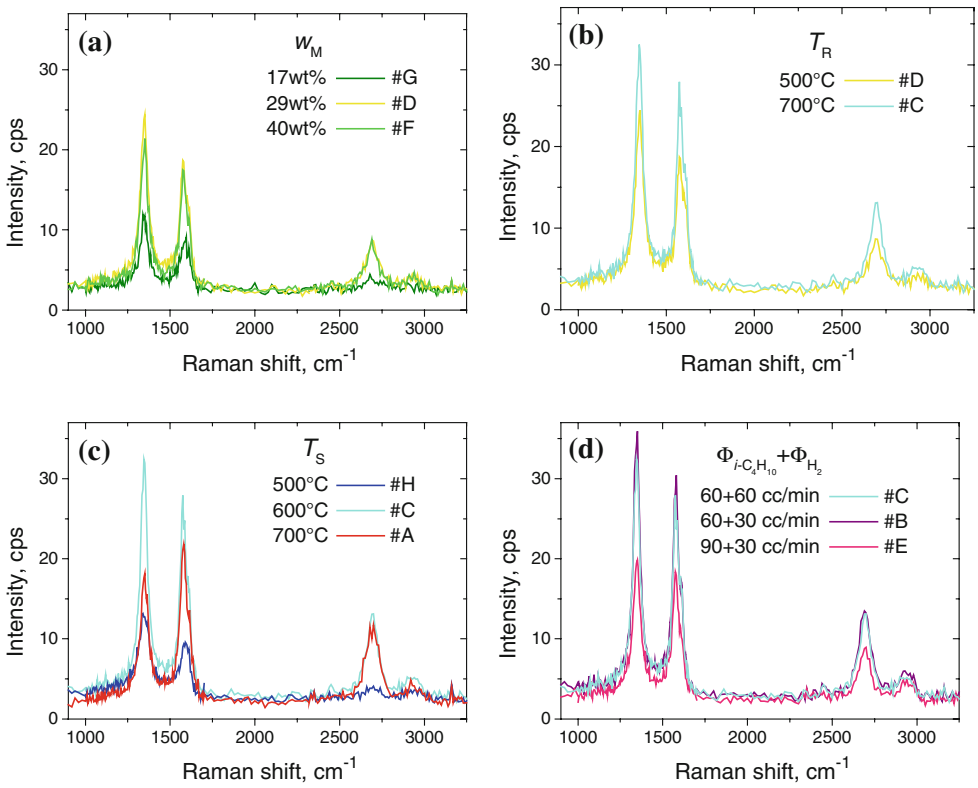

Fig. 4 Shape evolution undergone by the Raman spectra upon the variation of (**a**) metal load, (**b**) reduction temperature, (**c**) synthesis temperature and (**d**) growth ambient composition. For an easier comparison, the same vertical-axis scale is used

#H to #A as an effect of the decrease of defectiveness and of the development of smooth graphene layers, either *cylindrically rolled up* to form MWCNTs or *vertically piled* to constitute polycrystalline graphite flakes. Correspondingly, an intensification of the overall scattering intensity is noted (Fig. 4).

The indications emerging from RS analysis fully agree with those coming from the oxidation study: the sample resistance to oxidation is found to increase in the same order (Table 2). This is not surprising because the thermal stability is tightly related to the crystalline arrangement. As strictly concerns nanotubes, not only lattice defects at the tube end and along the outer walls act as initial oxidation sites but also the tube diameter and the wall thickness greatly affect their thermal stability [19, 20].

The existence of a correlation between the results of RS and TG measurements is clearly demonstrated in Fig. 5c, where the linear relationship between $I_{G'}/I_G$ and T_P is shown. Neglecting the small fraction of amorphous/disordered species (max: 5.2%), the thermal stability of the sample, as measured by the maximum-oxidation rate temperature in the DTG curves, increases as an effect of the *same* C deposit modifications which determine the intensifying of the G′-band relative to G-band in Raman spectra, namely the progressive development of long-range order in the tube- and/or flake-forming graphitic sheets.

Calibration of metal load: samples #D, #F and #G

Y_C shows a non-monotonic dependence on w_M (Table 1). The maximum is reached for $w_M = 29$ wt% (sample #D). Correspondingly, a noticeably high selectivity towards CNTs is achieved (Fig. 1b). The results of TG analysis (Table 2) indicate that the relative amount of Fe-inclusions is minimum (<4%) and the formation of by-products is negligible (<0.6%). The very thin MWCNTs exhibit good crystalline quality ($I_{G'}/I_D$ in Fig. 5b) and seem thermally stable up to 554 °C. Their combustion occurs in a quite narrow range ($\Delta T = 22$ °C), which is indicative of great structural homogeneity. This behaviour is in line with the existence of an optimal metal-load window [28, 29].

Varying Fe-load (samples #F and #G), the number of metal particles having optimal size, relative to the given C supply rate (CSR) [30, 31], diminishes. This has strong impact on selectivity, purity degree, and crystalline arrangement.

The relative amount of Fe-impurities increases because C layers coat metal particles whose size is out of the optimum size range (OSR) [30]. The growth becomes less selective, as proved by the increased amount of flakes-like formations detected by SEM. Also the TG analysis provides evidence of the major heterogeneity of C deposits at 17 and 40 wt%: their combustion occurs in a quite wider range ($\Delta T = 33$°C).

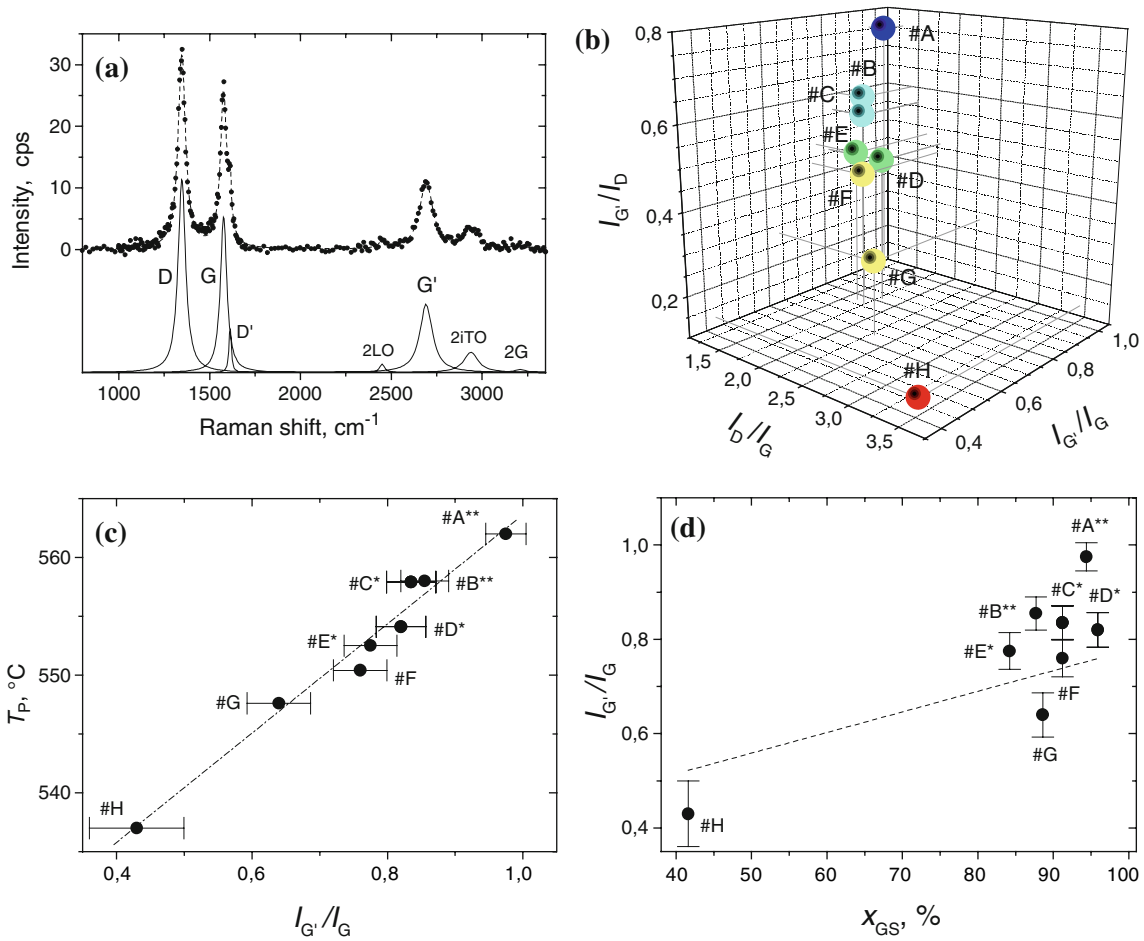

Fig. 5 (**a**) Raman spectra decomposition and (**b**) intensity ratios derived (the crystalline quality, as described by the G′/D intensity ratio, increases from sample #H to #A). (**c**) Correlation between TG, SEM and RS measurement results (*one* or *two stars* stand, respectively, for good and quite good selectivity towards nanotubes; the *dash-dotted line* is the best fit to the data). (**d**) Comparison with literature data (*dashed line*)

The reason for the diminishing of metal particles with optimal size is different in the two cases. Decreasing w_M from 29 to 17 wt% does not involve significant mean particle size changes, but only a commensurate reduction of sites available for CNT growth. Contrarily, as w_M increases from 29 to 40 wt%, the average diameter of iron crystallites, as estimated from the catalyst X-ray diffraction (XRD) patterns using Scherrer equation, increases by about a factor of 3/2 (from 19 to 28 nm); nonetheless, the overall metallic surface does not appreciably reduces (the variation is $\sim$8/9 in the spherical particle approximation) because the enlargement ($\sim$4/3) produced by the w_M increase compensates almost completely for the diminution ($\sim$2/3) originating from the particle size variation. Hence, in the former case, the effect of metal surface shrinking is seen, while in the latter that originating from the deviation from the OSR prevails.

In both the situations, the CSR successfully used over 29 wt% Fe-catalysts (134 mg/min, for $\Phi_{i-C_4H_{10}} = 60$ cc/min) becomes inadequate: excessive at $w_M = 17$ wt% and insufficient at $w_M = 40$ wt%. In the former case (sample #G), the growth is faster and gives rise to highly defective species. Drastic G′-band weakening and I_D/I_G ratio enhancement reflect loss of long-range order and increase of lattice defects. As a result, the crystalline quality ($I_{G'}/I_D$) lowers and the oxidation resistance ($T_P = 548$ °C) of C deposits reduces. Instead, at $w_M = 40$ wt% (sample #F), crystalline quality ($I_{G'}/I_D$) and thermal stability (T_P) undergo a slight improvement, because they benefit from the growth-rate lowering deriving from the longer diffusion length into the larger particle size [29].

Choice of reduction temperature: samples #C and #D

As previously observed for the growth of CNTs over Fe/SiO_2 catalysts in C_2H_6–H_2 atmosphere [1], the increase of T_R does not involve large change in selectivity. Contrarily, C yield diminishes by more than a factor of 2 (compare

samples #C and #D in Table 1). The causes of the drastic drop might be the increase of average particle size, signalled by narrowing and intensifying of metallic-iron peak in XRD pattern of catalyst reduced at 700 °C, and the chemical transformations, leading to the change of iron oxidation state for $T_R > 500$ °C [29, 32]. Since the CNT diameter mirrors the catalyst particle size [31], the tube thickening, evidenced by the morphologic study, corroborates the first hypothesis.

Evidently, the deviation from the OSR is not so large to hinder the CNT formation: C supply still suffices, but the C-polymerisation over the metal surface is more favoured [29, 33]. On one hand, this leads to larger amounts of Fe-inclusions and reaction by-products (Table 2), while, on the other hand, it reflects on slower growth rate, which is beneficial for crystalline quality (Fig. 5b). Actually, the increase of Raman-scattering intensity signals topological ordering (Fig. 4b). A lesser extent of lattice defects forms inside the slightly smoother sheets, and, as a result, in spite of the poorer yield and the worse purity degree, C deposits seem not only thermally stable up to higher temperature ($T_P = 558$ °C) but also endowed with similar homogeneity degree, as demonstrated by TG ($\Delta T = 24$ °C) and TEM analyses (sample #C in Fig. 2).

Tuning of synthesis temperature: samples #A, #C and #H

As expected, Y_C sizeably improves with the increase of synthesis temperature (compare samples #A, #C and #H in Table 1). At $T_S = 500$ °C, the slow C diffusion rate (CDR) represents the rate-limiting step. As CSR exceeds CDR, the excess of C atoms deposit in amorphous phase on metal surface and growing nanotubes [34]. This accounts for the huge amount of C-encapsulated Fe-nanoparticles ($x_{EI} > x_{GS}$) and for the relatively large x_{AS} value (5.2%). The co-production of amorphous/disordered C species, resulting from the mass loss in the 200–400 °C region of thermograms (Table 2), is confirmed also by RS. The width of D-band (~ 70 cm^{-1}) in the spectrum of sample #H (Fig. 4c) is out of the range (30–60 cm^{-1}) typically measured in MWCNTs [35], indicating the presence of species with a certain amorphousness degree. Upon "CDR limited" regime, the formation of CNTs is hampered [34]. Yield is poor due to the massive early catalyst deactivation brought about by metal particle encapsulation. The sample heterogeneity originating from the scarce process selectivity reflects in the largest combustion range ($\Delta T > 35$ °C), while lack of long-range order and presence of large lattice defect extent determines the worst crystalline quality (Fig. 5b) and the lowest oxidative resistance ($T_P = 537$ °C).

At $T_S = 700$ °C, the situation is diametrically opposite. The increase of T_S favours the sintering of metal particles, as demonstrated by the enlargement of tube diameters (compare samples #A and #C in Fig. 2), but the rate of C diffusion and of hydrocarbon decomposition gets faster. The large Y_C value (above 1400%), the scarce formation of different phases and the small amount of Fe-impurities (Table 2) clearly demonstrate that the beneficial effects of the latter factor prevail. The broadening of metal particle size distribution leads to the formation of MWCNTs with less uniform diameters (Fig. 2), as monitored also by the higher heterogeneity index ($\Delta T = 28$ °C). Nevertheless, the CNT-forming graphene layers are extremely smooth and scarcely defective (the highest $I_{G'}/I_G$ and the lowest I_D/I_G ratios are measured in sample #A), so as the highest ($I_{G'}/I_D$) crystalline quality and, hence, the greatest resistance to oxidation ($T_P = 562$ °C) are achieved.

Adjusting of growth ambient composition: samples #B, #C and #E

As shown, carrying out reaction at moderate synthesis temperature (600 °C) over catalysts with 29 wt% Fe-load reduced at 700 °C allows achieving satisfactory crystalline quality and thermal stability (sample #C) by the use of 1:1 120 cc/min i-C_4H_{10}–H_2 gas mixture. Changing the growth ambient composition, a sizeable worsening in terms of yield (Table 1), selectivity and purity degree (Table 2) occurs.

With the reduction of the $\Phi_{H_2}/\Phi_{i-C_4H_{10}}$ flow ratio (from 1 in sample #C to 1/2 and 1/3 in samples #B and #E, respectively), the catalytic-activity preserving action by H_2 [36] gradually diminishes and the carbon polymerisation over the metal surface is increasingly favoured [29, 33]. This causes iron encapsulation to progressively increase from 7.3 to 15.2%, while the fraction of supplied carbon transformed to deposits [37] simultaneously declining from 13.7% in sample #C down to 9.2 and 6.2% in samples #B and #E, respectively. The continuous decrease of x_{GS} (from 91 to 84%) and x_{AS} (from 1.5 to 0.6%) proves that, under these conditions, both graphitically ordered and amorphous/disordered C species form more hardly.

As suggested by the variations of the heterogeneity index (see ΔT in Table 2) and confirmed by the examination of the C deposit morphology, the worsening in selectivity is more pronounced when the $\Phi_{H_2}/\Phi_{i-C_4H_{10}}$ flow rate is reduced from 1/2 to 1/3. As can be seen in Fig. 1g, large carbonaceous terrace flakes are copiously produced in sample #E. The higher CSR ($\Phi_{i-C_4H_{10}} = 90$ cc/min) promotes the formation of lattice defects, while the surface diffusion lowering brought about by the $\Phi_{H_2}/\Phi_{i-C_4H_{10}}$ diminishing hinders the long-range graphitic ordering (Fig. 5b). The consequent crystalline-arrangement downgrade reflects in a general Raman intensity weakening (Fig. 4d) and in a T_P downshift (553 °C). Contrarily, moving from sample #C ($\Phi_{H_2} = 60$ cc/min) to #B ($\Phi_{H_2} = 30$ cc/min), the

crystalline quality ($I_{G'}/I_D$) undergoes a small improvement because the extent of lattice defects (I_D/I_G) slightly reduces thanks to the growth rate lowering, while the long-range order ($I_{G'}/I_G$) enhances a bit owing to the unselective formation of graphitic plaques.

Correlation between TG and RS analysis results

From the above discussion it clearly emerges that selectivity towards CNTs, crystalline quality and oxidative resistance, as, respectively, assessed by SEM, RS and TG analyses, increase in the same order, as reasonably expected (Fig. 5c). Besides, a linear relationship is observed between $I_{G'}/I_G$ and T_P.

Recently, DiLeo et al. [24] have proposed the use of RS for the MWCNT purity assessment. They have shown that the parameters derived by decomposing 2.54 eV Raman spectra are tightly correlated with the MWCNT content (0–100%) of samples suitably prepared by mixing known amounts of carbonaceous by-products and MWCNTs *separately* attained under two diverse reaction conditions. The authors have shown that the calibration curves, attained by plotting I_D/I_G, $I_{G'}/I_G$ and $I_{G'}/I_D$ as a function of the constructed-sample MWCNT content, allow successfully assessing the purity degree of the samples they grow under different conditions.

In samples "as-obtained" from synthesis (present case), plotting I_D/I_G, $I_{G'}/I_G$ and $I_{G'}/I_D$ gives consistent, but, by far, less sharp trends: for instance, as demonstrated in Fig. 5d, only a wide spread increase of $I_{G'}/I_G$ with x_{GS} is observed in place of the linear growth reported [24]. This is not only because, as above discussed, x_{GS} includes *all* the C species with graphitic ordering (MWCNTs and flakes), but also because, even in cases (marked by stars in Fig. 5d) where almost exclusively MWCNTs are attained, their outer diameters, wall thickness and diameter distribution change with changing the growth conditions, differently from the samples "constructed", where only the relative abundance of MWCNTs varies [24]. Indeed, as the measured intensity ratios are the result of the superposition of the effects arising from *all* the cited changes, the effect brought about by each of them can be hardly singled out.

Excepting for single-walled carbon nanotubes and a few of other nanostructures, such as carbon nano-onions, having quite peculiar spectral fingerprints [21, 22, 38], single excitation-wavelength Raman spectroscopy, alike thermogravimetric analysis, is not always really able to distinguish between the various form of graphitically-organised carbon. In such cases, the aid of complementary techniques (such as SEM), or the use of novel operative procedures [12], is necessary for their identification. Instead, since it is sensitive to the same modification of crystalline arrangement, which determine the change of thermal stability, RS may be used for the *quick and non-destructive* preliminary sample evaluation, with no need of performing the time-expensive TG investigation.

Conclusions

The growth of MWCNTs by CCVD is considered. The synthesis reaction is carried out in 120 cc/min *i*-C_4H_{10}–H_2–He atmosphere, at temperature ranging from 500 to 700 °C, by varying *i*-C_4H_{10} (60–90 cc/min) and H_2 (30–60 cc/min) flow rates as well as metal load (17–40 wt%) and reduction temperature (500 and 700 °C) of Fe/Al_2O_3 catalysts. The selectivity of the growth process towards nanotubes is evaluated by SEM, the thermal stability of the C deposits is assessed by TG and the results of Raman analysis are used as a guide for the calibration of the parameters involved for purpose of maximising the crystalline quality of the MWCNTs attained. It is so found that the best results are obtained by the use of 29 wt% Fe catalysts reduced at 700 °C. The highest oxidative resistance and the best crystalline quality are achieved carrying out the synthesis reaction at 700 °C in 1:1:0 *i*-C_4H_{10}–H_2–He atmosphere. At lower synthesis temperatures (600 °C), still satisfactory results can be attained using the same gas mixture composition. However, while in the former case more than 14 g of 94%-purity CNTs per gram of catalyst are attained; in the latter, yield undergoes a drastic drop and purity worsens: only ~4 g of 91%-purity CNTs per gram of catalyst are produced.

The most important outcome of this study is that the thermal stability, as measured by the maximum-oxidation rate temperature in the differential TG curves, increases as an effect of the same C deposit modifications which determine the intensifying of the G′-band relative to G-band in Raman spectra. The progressive establishing of the long-range graphitic order due to the development of smooth graphene layers—cylindrically rolled up to form MWCNTs and/or vertically piled to constitute polycrystalline graphite flakes—seems to be mainly responsible for the peak temperature up-shift. This suggests using RS, coupled to SEM analysis, for the quick and non-destructive preliminary sample evaluation in terms of thermal stability, rather than performing time-expensive TG measurements.

References

1. Iijima S (1991) Nature 354:56
2. Choi WB, Chung DS, Kang JH, Kim HY, Jin YW, Han IT, Lee YH, Jung JE, Lee NS, Park GS, Kim JM (1999) Appl Phys Lett 75:3129
3. Lee SM, Lee YH (2000) Appl Phys Lett 76:2877
4. Wang S (2004) Electroanalysis 17:7

5. Raghuveer MS, Ganesan PG, D'Arcy-Gall J, Ramanath G, Marshall M, Petrov I (2004) Appl Phys Lett 84:4484
6. Harrison BS, Atala A (2007) Biomaterials 28:344
7. Reich S, Thomsen C, Maultzsch J (2004) Carbon nanotubes. Wiley-VCH, Berlin
8. Lee K, Zhang J, Wang H, Wilkinson DP (2006) J Appl Electrochem 36:507
9. Musumeci A, Silva G, Martens W, Waclawik E, Frost R (2007) J Therm Anal Calorim 88:885
10. Trigueiro JP, Silva GG, Lavall RL, Furtado CA, Oliveira S, Ferlauto AS, Lacerda RG, Ladeira LO, Liu JW, Frost RL, George GA (2007) J Nanosci Nanotechnol 7:3477
11. Silva GG, Musumeci AW, Gomes AP, Liu JW, Waclawik ER, George GA, Frost RL, Pimenta MA (2009) J Mater Sci 44:3498. doi:10.1007/s10853-009-3468-x
12. Gozzi D, Latini A, Lazzarini L (2008) Chem Mater 20:4126
13. Zhao X, Ando Y, Qin LC, Kataura H, Maniwa Y, Saito R (2002) Appl Phys Lett 81:2550
14. Santangelo S, Messina G, Donato MG, Lanza M, Milone C, Pistone A (2006) J Appl Phys 100:104311
15. Donato MG, Galvagno S, Messina G, Milone C, Pistone A, Santangelo S (2007) Diam Relat Mater 16:1095
16. Messina G, Santangelo S, Donato MG, Lanza M, Milone C, Pistone A, Galvagno S (2008) Phys Stat Sol 205:2422
17. Li Q, Yan H, Zhang J, Liu Z (2004) Carbon 42:829
18. Kitiyanan B, Alvarez WE, Harwell JH, Resasco DE (2000) Chem Phys Lett 317:497
19. Bom D, Andrews R, Jacques D, Anthony J, Chen B, Meier MS, Selegue JP (2002) Nano Lett 2:615
20. Pang LSK, Saxby JD, Chatfield SP (1993) J Phys Chem 97:6941
21. Kuzmany H, Burger B, Thess A, Smalley R (1998) Carbon 36:709
22. Dresselhaus MS, Dresselhaus G, Saito R, Jorio A (2005) Phys Rep 409:47
23. Kim YA, Hayashi T, Osawa K, Dresselhaus MS, Endo M (2003) Chem Phys Lett 380:319
24. DiLeo RA, Landi BJ, Raffaelle RP (2007) J Appl Phys 101:64307
25. Ferrari AC, Robertson J (2001) Phys Rev B 61:14095
26. Ferrari AC, Robertson J (2001) Phys Rev B 64:75414
27. Thomsen C, Reich S (2000) Phys Rev Lett 85:5214
28. Tsoufis T, Xidas P, Jankovic L, Gournis D, Saranti A, Bakas T, Karakassides MA (2007) Diam Relat Mater 16:155
29. Yu Z, Chen D, Tødtal B, Holmen A (2005) Catal Today 100:261
30. Ducati C, Alexandrou I, Chhowalla M, Amaratunga GA, Robertson J (2002) J Appl Phys 92:3299
31. Ducati C, Alexandrou I, Chhowalla M, Robertson J, Amaratunga GAJ (2004) J Appl Phys 95:6387
32. Neri G, Visco AM, Galvagno S, Donato A, Panzalorto M (1999) Thermochim Acta 329:39
33. Chen D, Christensen KO, Ochoa-Fernandez E, Yu Z, Tødtal B, Latorre N, Monzon A, Holmen A (2005) J Catal 229:82
34. Juang ZY, Lai JF, Weng CH, Lee JH, Lai HJ, Lai TS, Tsai CH (2004) Diam Relat Mater 13:2140
35. Belin T, Epron F (2005) Mater Sci Eng B 119:105
36. Choi GS, Cho YS, Hong SY, Park JB, Son KH, Kim DJ (2002) J Appl Phys 91:3847
37. Donato MG, Messina G, Milone C, Pistone A, Santangelo S (2008) Diam Relat Mater 17:318
38. Roy D, Chhowalla M, Wang H, Sano N, Alexandrou I, Clyne TW, Amaratunga GAJ (2003) Chem Phys Lett 373:52